Vibration Analysis of Curved Panel Subjected to Internal Pressure and Axial Compression

Vibration and buckling analysis of curved panel subjected to combined internal pressure and axial compression

Fangzhou Zhu[a,b,*], Riccardo Augello[b,†], Rodolfo Azzara[b,‡], Alfonso Pagani[b,§], Erasmo Carrera[b,¶] and Weiqiu Chen [a,c,‖]

[a] *Key Laboratory of Soft Machines and Smart Devices of Zhejiang Province and Department of Engineering Mechanics, Zhejiang University, Hangzhou, 310027, PR China*

[b] *Department of Mechanical and Aerospace Engineering, Politecnico di Torino, 10129, Torino, Italy*

[c] *Shenzhen Research Institute of Zhejiang University, Shenzhen, PR China*

This paper discusses the change of the natural frequencies and the corresponding mode shapes of an isotropic metallic curved panel subjected to combined internal pressure and axial compression. Tensor calculus is employed to devise the differential operator matrices of the geometrical relation in an orthogonal curvilinear reference system. In the framework of Carrera Unified Formulation (CUF) and applying the finite element method, the principle of virtual work is utilized to describe the free vibration of a cylindrical shell subjected to progressive external loading conditions, as a virtual procedure of the experimental test Vibration Correlation Technique (VCT). Finally, numerical examples are provided, and the effects of the material and geometric characteristics are evaluated. The results show that crossing and veering phenomena between natural frequencies appear when varying the curvature of the panel and the value of the inner pressure, and those effects have to be taken into account for a proper design of this type of structure.

I. Nomenclature

$\mathbf{B}_l$	=	linear algebraic matrices
$\mathbf{E}_L$	=	young's module of the loading part
$\mathbf{E}_R$	=	young's module of the research object
F_τ	=	expansion functions along the thickness coordinate z
$\mathbf{K}_s^{ij\tau s}$	=	fundamental nucleus of the secant stiffness matrix
$\mathbf{K}_\sigma^{ij\tau s}$	=	geometric stiffness
$\mathbf{L}_{ine}$	=	work of the inertia loads

*Ph.D student, Department of Engineering Mechanics,Zhejiang University, Hangzhou, 310027, PR China.

†Postdoc, Department of Mechanical and Aerospace Engineering, Politecnico di Torino, 10129 Torino, Italy

‡Ph.D student, Department of Mechanical and Aerospace Engineering, Politecnico di Torino, 10129 Torino, Italy

§Associate professor, Department of Mechanical and Aerospace Engineering, Politecnico di Torino, 10129 Torino, Italy

¶Professor, Department of Mechanical and Aerospace Engineering, Politecnico di Torino, 10129 Torino, Italy

‖Professor, Department of Engineering Mechanics,Zhejiang University, Hangzhou, 310027, PR China.

$\mathbf{L}_{int}$ = strain energy

$\mathbf{M}_{ij\tau s}$ = fundamental nucleus of the mass matrix

N = order of the expansion in thickness direction

N_i = shape function

$\mathrm{P}_{\mathrm{inner}}$ = inner pressure

R_α, θ = radius and curvature

$\mathbf{u}_\tau, \mathbf{u}_{\tau i}$ = generalized displacement vector and finite element nodal parameters

α, β, z = two in-plane coordinates and one through-thickness coordinate

δ = variation

$\boldsymbol{\epsilon}$ = strain vector

ω = angular frequency

II. Introduction

In modern industries, thin-walled structures and curved shells are extensively used as load-bearing units for various applications, for instance in the manufacture of storage tanks, launch vehicles, pressure vessels, airplane wings, among the others. Thanks to their outstanding engineering properties, such as high stiffness-weight and strength-weight ratios, curved shell structures are capable of operating in complex working environments, especially under combined loading conditions. For example, shells of rocket propellant tanks are subjected to internal and external pressure and axial compression [1]. Pipelines installed by horizontal directional drilling are usually subjected to a combination of tension, blending, and external pressure [2]. Composite pressure vessels usually work under combined mechanical and hygrothermal loadings [3]. The capability of maintaining their shape and the support loads improves its popularity in manufacturing. Moreover, due to its structural continuity, shell structures can transmit the loads in a number of different directions. Therefore, shell structures attracted scientists' interest and were theoretically and experimentally investigated for the past several decades [4–7].

Due to the large operational combined loads, curved shell structures may be subjected to large displacements and rotations, or to internal stresses that eventually alter the rigidity of the structure. Considering the real complex working condition, there are numerous works concentrating on the investigation of buckling behaviours and modal shapes detecting of shell structures. Date back to 1960s, Hess [8] and Cheng [9] et al. established the analytical formulas for cylindrical shells under combined loading conditions which are of significant reference value. After that, Pope [10] presented a finite-deflection analysis for the buckling of long and slightly curved panels in compression under various boundary conditions. Osamu [11] presented an approximate theoretical analysis of the post-buckling behavior of a finite thin curved panel uniformly compressed in the axial direction and subjected to simply-support boundary conditions,

using a trigonometric function. Shen [12, 13] theoretically investigated the buckling and post-buckling behavior of shear deformable cross-ply laminated cylindrical shells subjected to combined external pressure and axial compression and pointed out three impact factors, i.e. geometric, loading and imperfection parameters. K.Y.Lam [14] compared four different shell theories in the study of dynamic stability of simply supported, thin, isotropic cylindrical shells under combined static and periodic axial forces and accessed the agreement similarities among these shell theories. Experimental investigation of the buckling and post-buckling of CFRP shells under combined axial and torsion loading was conducted by Chiara [15] and he highlighted the independence between the buckling loads and the load sequence and demonstrated the load sustainability of shell structures in the post-buckling field without any damage. Fahimeh [16] theoretically investigated the size-dependent buckling of anisotropic piezoelectric cylindrical shells and pointed out that the critical buckling load is found to be significantly size-dependent.

The vivid interest of the literature on the buckling of curved panels, demonstrate the importance of accurately evaluating that condition. Among the experimental approaches, the Vibration Correlation Technique (VCT) represents a reliable analysis. It consists of a non-destructive approach for evaluating the first critical buckling load, by interpolating the natural frequencies of the structure subjected to progressive loadings, without reaching the instability point and it was actively employed for decades[17, 18]. The idea of VCT that combines vibration characteristics with buckling load was proposed by Sommerfeld[19]. He tested a clamped-free column and observed that the natural frequency of the column decreased and approached to zero as the tip mass reached the buckling weight. Later on, theoretical and experimental investigations on the buckling vibration relation were carried out to evaluate the theories and establish practical nondestructive VCTs by several researchers[20–24]. In particular, Lurie[25] theoretically and experimentally investigated the vibration characteristics on elastically restrained columns in the form of rigid rectangular frames and he demonstrated the practical feasibility of VCT to predict the buckling load that the relationship between the square of the frequency and the load is practically linear, and the extrapolated load corresponding to zero frequency coincides with the buckling load. This property gives a good approximation to the buckling load. A detailed review of the VCT approach on different structures can be found in Chapter 15 of Singer et al.'s work[26]. Additionally, there are many works on the buckling load estimation recently which is of great referential value[27–30].

Most of the published works regarding the application of VCT focusses on the cylindrical shells[31, 32]. In the present work, the change of natural frequencies and associated mode shapes in metallic panels subjected to combined internal and compressive loads is investigated. To develop such analysis, a virtual VCT is performed and the Carrera Unified Formulation (CUF) along with the Finite Element Method (FEM) is employed to build the mathematical models. Similar analyses were already succesfully developed in the contest of CUF for isotropic [33, 34] and composite [35] beams. Here, the formulation is further extended to deal with curved panels.

The present work is organized as follows: (1) Brief introductory information including CUF expansions and the relevant finite element are given in Section III;(2) Then, numerical examples are reported and discussed in Section IV to evaluate

the performance of the employed numerical-based VCT. The change of natural frequency and relative mode shapes are illustrated. Three impact factors E_L/E_R , P_{inner}, R_α and θ are detailed studied;(3) finally, the concluding remarks are listed in Section V.

III. CUF, FEM and VCT analysis of free vibration of the curved shell structures

Consider a curved shell structure, which is represented by an orthogonal curvilinear reference system (α, β, z). The α and β denote two in-plane coordinates and z denotes the through-the-thickness coordinate, as shown in Fig. 1. The constitutive expressions for elastic metallic materials and the Green-Lagrange geometrical relations can be found in many literatures [36, 37] aren't listed here for the sake of brevity. According to CUF, the 3D displacement field $\mathbf{u}(\alpha, \beta, z)$ of the shell structure can be directly written as:

$$\mathbf{u}(\alpha, \beta, z) = F_\tau(z)\,\mathbf{u}_\tau(\alpha, \beta), \qquad \tau = 0, 1, 2, ..., N, \tag{1}$$

where F_τ are the expansion functions of the thickness coordinate z, $\mathbf{u}_\tau$ is the generalized displacement vector depending on the in-plane coordinates α and β, N denotes the order of the expansion in the thickness direction, and the summing convention regarding the repeated index τ is adopted. The choice of F_τ and N is purely arbitrary and can be decided as input parameters for the mathematical model. Different base functions (such as Lagrange expansions, Taylor expansions, hierarchical Legendre expansions) of any order can be adopted to model the displacement field of shell structures over the thickness. In this paper, Lagrange polynomials are taken into account as F_τ functions along the thickness direction, and the so-called Lagrange Expansion CUF shell models are explicitly discussed in the book [38]. The considered shell theories are abbreviated by LDN, which represents the Lagrange expansion, Displacement-based theory with the order of expansion N. Specifically, the two-node linear (LD2), three-node quadratic (LD3) and four-node cubic (LD4) Lagrange expansion functions are employed along the thickness direction so as to formulate linear to higher-order kinematics CUF shell elements.

Independent of the considered shell theories, the Finite Element Method (FEM) is utilized to describe the generalized displacement vector $\mathbf{u}_\tau(\alpha, \beta)$ of the shell structure in the $\alpha - \beta$ plane by means of shape functions $N_i(\alpha, \beta)$ and it can be expanded as:

$$\mathbf{u}_\tau(\alpha, \beta) = N_i(\alpha, \beta)\,\mathbf{u}_{\tau i}, \qquad i = 1, 2, 3, ..., n_{el}, \tag{2}$$

where n_{el} represents the number of nodes per element and i indicates summation. The finite element nodal parameters $\mathbf{u}_{\tau i}$ are defined as:

$$\mathbf{u}_{\tau i} = \left\{ u_{\alpha_{\tau i}} \quad u_{\beta_{\tau i}} \quad u_{z_{\tau i}} \right\}^{\mathsf{T}} \tag{3}$$

The component form of shape functions $N_i\ (\alpha, \beta)$ are not presented here and interested readers can find them in many literature, for example in Bathe [39].

In this paper, the classic 2D nine-node quadratic FE (Q9) is adopted for the shape function in the $\alpha - \beta$ plane. For completeness, Fig. 1 shows the approximations for a typical curved shell. Then, combining CUF and FEM, the strain vector utilized in this paper is formulated as:

$$\boldsymbol{\epsilon} = \mathbf{B}_l\, \mathbf{u}_{\tau i} \tag{4}$$

where $\mathbf{B}_l$ represents the linear algebraic matrices.

The principle of virtual works is utilized to describe the free vibration of the curved shells.

$$\delta L_{int} = -\delta L_{ine} \tag{5}$$

where L_{int} is the strain energy, L_{ine} is the work of the inertia loads, and δ signifies the variation. Substituting geometrical relation and the constitutive law into eq. (5), the virtual variation of the strain energy can be written as:

$$\delta L_{int} = \delta \mathbf{u}_{sj}^{\mathsf{T}} \mathbf{K}_0^{ij\tau s} \mathbf{u}_{\tau i} \tag{6}$$

Moreover, the fundamental nucleus of the linear mass matrix is derived from the virtual variation of the inertia loads:

$$\delta L_{ine} = \delta \mathbf{u}_{sj}^{\mathsf{T}} \mathbf{M}^{ij\tau s} \ddot{\mathbf{u}}_{\tau i} \tag{7}$$

where the $\mathbf{M}^{ij\tau s}$ represents the fundamental nucleus of the mass matrix. Considering that the analysis of the vibration of the curved shell is performed around a linearized state of equilibrium, the virtual variation of the inertial loads is assumed to be linear and the tangent stiffness matrix can be computed from the virtual variation of the strain energy:

$$\delta\left(\delta L_{int}\right) = \delta \mathbf{u}_{sj}^{\mathsf{T}} \mathbf{K}_0^{ij\tau s} \mathbf{u}_{\tau i} + \delta \mathbf{u}_{sj}^{\mathsf{T}} \mathbf{K}_\sigma^{ij\tau s} \mathbf{u}_{\tau i} = \delta \mathbf{u}_{sj}^{\mathsf{T}} \mathbf{K}_T^{ij\tau s} \mathbf{u}_{\tau i} \tag{8}$$

where $\mathbf{K}_\sigma^{ij\tau s}$ represents the *geometric stiffness*. The detailed derivation of the stiffness fundamental nucleus are listed in the work [40]. In order to obtain the non-trivial solutions, the equation of motion can be simplified into a linear problem:

$$\left(\mathbf{K}_T^{ij\tau s} - \omega^2 \mathbf{M}^{ij\tau s}\right) \mathbf{u}_{\tau i} = 0 \tag{9}$$

IV. Numerical examples and discussions

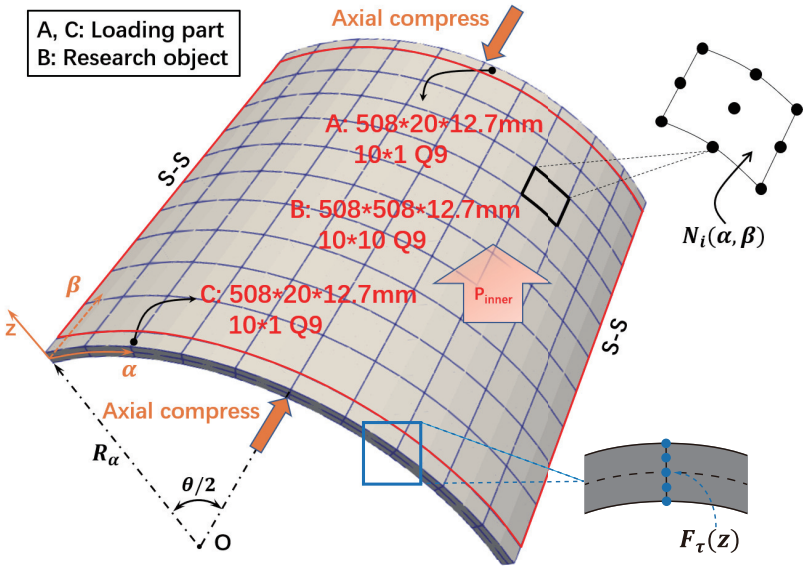

Fig. 1 Geometrical description of an isotropic curved shell subjected to combined internal pressure (P_{inner}) and axial compression (P_{axial}) in the underformed configuration along with the FE discretization and CUF kinematics.

This section discusses the effect of the three impact factors shown in Eq. (10), i.e. the ratios between the Young moduli of the loading domain and the research object, the internal pressure, the radius and the central angle,

$$E_L/E_R\,, \quad P_{inner}, \quad R_\alpha \text{ and } \theta \tag{10}$$

Moreover, numerical calculations are conducted to exhibit the capabilities of the virtual linearized VCT theory for detecting the modal shape and predicting buckling load of curved shells subjected to combined internal pressure and axial compression.

As fas ar the geomteric and material properties are concerned, the isotropic curved shell involves an aluminum panel, of which geometrical size is $508 \times 508 \times 12.7$mm (arclength $\times$ width $\times$ thickness), and two loading areas are $508 \times 20 \times 12.7$mm, attached to two opposite sides of the panel. In real working condition, the uniform axial pressure requires a pair of opposite fixures to be applied on the edges of the curved shell. Simply supported boundary conditions are applied on the other two sides. Material properties of the research object are $E_R = 70.0 \times 10^3 \text{N/mm}^2$, $\nu = 0.33$, $\rho = 2700\text{kg/m}^3$. The radius $R_\alpha = 2540.01$mm and the central angle $\theta = 0.2$.

In this analysis, classical 2D nine-node quadratic FEs (Q9) are chosen for the shape function $N_i(\alpha, \beta)$ of the curved shell in the $\alpha - \beta$ plane. For the research object, 10×10Q9 element is chosen for the in-plane mesh and 2×LD2 element for the thickness, whereas 1×10Q9 element is employed for the loading part.

A. Effect of the ratios between the loading part and the research object (E_L/E_R)

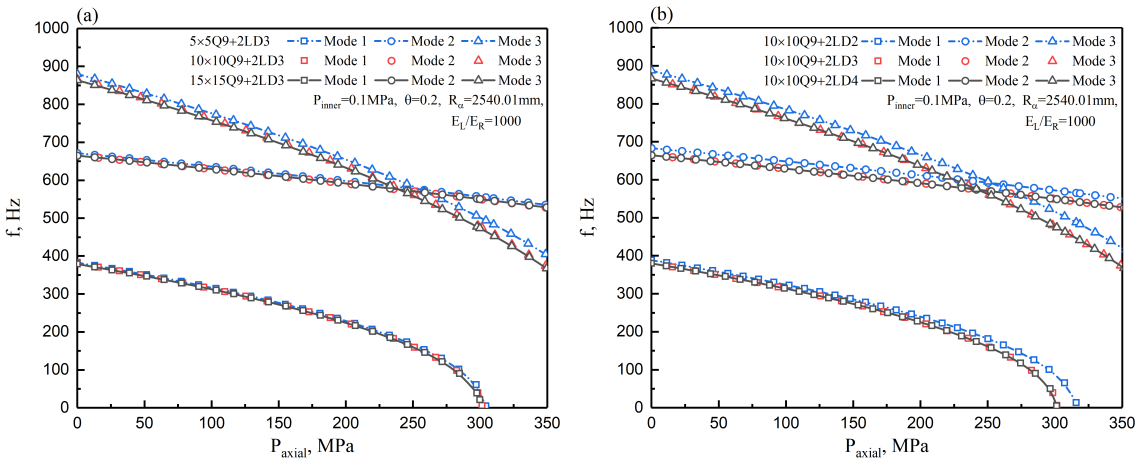

Fig. 2 Convergence analysis of equilibrium curves for the simple-supported isotropic curved shell under combined internal pressure and axial compression. (a) Comparison of different in-plane mesh numbers; (b) comparison of various orders of Lagrange expansion functions in the thickness direction.

Table 1 Equilibrum points (P_{axial}, f) of VCT response curves of the simple-supported curved shell under combined internal pressure and axial compression with *different in-plane mesh numbers*.

Mesh number + Expansion order (DOFs)												
5 × 5Q9 + 2LD3				10 × 10Q9 + 2LD3				15 × 15Q9 + 2LD3			
P_{axial}/MPa	f_1/Hz	f_2/Hz	f_3/Hz	P_{axial}/MPa	f_1/Hz	f_2/Hz	f_3/Hz	P_{axial}/MPa	f_1/Hz	f_2/Hz	f_3/Hz
0	382.908	671.417	880.222	0	380.037	665.076	866.796	0	379.066	665.061	863.993
12.917	375.132	666.994	867.582	15.702	370.516	659.665	851.149	12.941	371.239	660.616	851.100
25.833	367.164	662.535	854.736	31.404	360.704	654.199	835.180	25.882	363.217	656.136	837.991
38.75	358.990	658.039	841.675	47.106	350.576	648.678	818.871	38.824	354.986	651.617	824.654
51.667	350.595	653.504	828.388	62.809	340.101	643.098	802.199	51.765	346.531	647.061	811.078
64.583	341.960	648.930	814.863	78.511	329.242	637.459	785.140	64.706	337.833	642.466	797.249
77.5	333.066	644.315	801.087	94.213	317.958	631.759	767.667	77.647	328.870	637.830	783.154
90.417	323.889	639.659	787.048	109.915	306.197	625.994	749.750	90.589	319.620	633.153	768.778
103.334	314.402	634.960	772.730	125.617	293.898	620.164	731.356	103.53	310.054	628.433	754.103
116.25	304.576	630.218	758.116	141.319	280.986	614.265	712.445	116.471	300.139	623.669	739.112
129.167	294.373	625.429	743.189	157.021	267.367	608.294	692.975	129.412	289.839	618.860	723.784
142.084	283.749	620.595	727.929	172.723	252.920	602.250	672.895	142.354	279.106	614.005	708.096
155	272.654	615.712	712.313	188.426	237.486	596.130	652.147	155.295	267.887	609.101	692.024
167.917	261.023	610.780	696.316	204.128	220.849	589.929	630.662	168.236	256.112	604.149	675.538
180.834	248.778	605.796	679.912	219.83	202.702	583.645	608.362	181.177	243.699	599.145	658.606
193.75	235.818	600.760	663.068	235.532	182.581	577.275	585.151	194.119	230.539	594.088	641.194
206.667	222.014	595.669	645.750	251.234	159.726	570.813	560.913	207.06	216.490	588.977	623.258
219.584	207.190	590.521	627.916	266.936	132.704	564.257	535.505	220.001	201.360	583.809	604.751
232.5	191.104	585.315	609.522	282.638	98.096	557.601	508.750	232.942	184.875	578.583	585.619
245.417	173.396	580.048	590.513	298.341	39.261	550.841	480.418	245.884	166.624	573.297	565.795
258.334	153.494	574.719	570.826	301.38	5.862	549.520	474.729	258.825	145.934	567.947	545.203
271.251	130.387	569.324	550.387					271.766	121.550	562.532	523.751
284.167	101.896	563.861	529.108					284.707	90.509	557.050	501.326
297.084	60.850	558.328	506.882					297.649	39.299	551.496	477.790
304.24	5.144	555.231	494.113					297.678	39.105	551.484	477.735
								299.771	21.163	550.579	473.814

Table 2 Equilibrum points (P_{axial}, f) of VCT response curves of the simple-supported curved shell under combined internal pressure and axial compression with *various expansion orders*.

Mesh number + Expansion order (DOFs)												
10 × 10Q9 + 2LD2				10 × 10Q9 + 2LD3				10 × 10Q9 + 2LD4			
P_{axial}/MPa	f_1/Hz	f_2/Hz	f_3/Hz	P_{axial}/MPa	f_1/Hz	f_2/Hz	f_3/Hz	P_{axial}/MPa	f_1/Hz	f_2/Hz	f_3/Hz
0	388.473	683.235	888.026	0	380.037	665.076	866.796	0	380.013	664.813	866.693
11.376	381.763	679.426	877.009	15.702	370.516	659.665	851.149	10.98	373.385	661.033	855.785
22.752	374.914	675.591	865.838	31.404	360.704	654.199	835.180	21.96	366.618	657.227	844.723
34.127	367.919	671.730	854.507	47.106	350.576	648.678	818.871	32.939	359.705	653.394	833.499
45.503	360.768	667.841	843.009	62.809	340.101	643.098	802.199	43.919	352.635	649.534	822.108
56.879	353.450	663.925	831.338	78.511	329.242	637.459	785.140	54.899	345.399	645.646	810.542
68.255	345.955	659.981	819.485	94.213	317.958	631.759	767.667	65.879	337.985	641.729	798.792
79.63	338.270	656.008	807.443	109.915	306.197	625.994	749.750	76.859	330.380	637.782	786.851
91.006	330.380	652.005	795.202	125.617	293.898	620.164	731.356	87.839	322.569	633.806	774.709
102.382	322.269	647.972	782.752	141.319	280.986	614.265	712.445	98.818	314.536	629.798	762.357
113.758	313.918	643.908	770.084	157.021	267.367	608.294	692.975	109.798	306.262	625.759	749.782
125.134	305.308	639.812	757.185	172.723	252.920	602.250	672.895	120.778	297.725	621.688	736.974
136.509	296.413	635.684	744.043	188.426	237.486	596.130	652.147	131.758	288.901	617.583	723.920
147.885	287.205	631.522	730.645	204.128	220.849	589.929	630.662	142.738	279.761	613.445	710.606
159.261	277.652	627.326	716.976	219.83	202.702	583.645	608.362	153.718	270.271	609.271	697.015
170.637	267.715	623.096	703.019	235.532	182.581	577.275	585.151	164.697	260.391	605.062	683.133
182.013	257.346	618.829	688.757	251.234	159.726	570.813	560.913	175.677	250.071	600.816	668.938
193.388	246.489	614.525	674.170	266.936	132.704	564.257	535.505	186.657	239.252	596.532	654.411
204.764	235.074	610.183	659.234	282.638	98.096	557.601	508.750	197.637	227.860	592.209	639.529
216.14	223.011	605.802	643.927	298.341	39.261	550.841	480.418	208.617	215.802	587.846	624.264
227.516	210.184	601.381	628.219	301.38	5.862	549.520	474.729	219.596	202.953	583.442	608.589
238.891	196.441	596.918	612.079					230.576	189.149	578.995	592.469
250.267	181.568	592.413	595.471					241.556	174.157	574.504	575.865
261.643	165.254	587.864	578.354					252.536	157.631	569.968	558.736
273.019	147.012	583.269	560.681					263.516	139.019	565.386	541.028
284.395	125.999	578.628	542.395					274.496	117.319	560.755	522.683
295.77	100.479	573.938	523.433					285.475	90.318	556.075	503.629
307.146	65.345	569.199	503.716					296.455	50.043	551.343	483.783
315.776	13.505	565.569	488.198					301.338	5.040	549.221	474.676

The first numerical example is performed to investigate the effect of the ratios between the loading part and the research object (E_L/E_R). For convergence analysis, equilibrium curves for the simple-supported isotropic curved shell under combined internal pressure (P_{inner}) and axial compression (P_{axial}) is illustrated in Fig. 2 for different in-plane mesh numbers(Fig. 2(a)) and various orders of Lagrange expansion functions in the thickness direction (i.e., LD2, LD3 and LD4 as shown in Fig. 2(b)). It can be seen from Fig. 2(a) that the convergence is obtained quickly with the increase of the number of the in-plane mesh. In addition, Fig. 2(b) demonstrates that a quadratic of Lagrange expansion(i.e. LD3) can predict the equilibrium curves with excellent convergence rates. Additionally, in order to provide the reference solutions of different in-plane meshes and expansion orders for future comparison, the equilibrium points for the simple-supported isotropic curved shell under combined internal pressure and axial compression are tabulated in Table 1 and 2.

From the perspective of experiment and simulation, two loading parts are attached to the isotropic aluminum curved shell so as to apply uniform pressure in axial direction. However, different kinds of attached loading parts strongly and directly influence the original boundary condition of the research object. In this part, it is discussed how the loading part affects the natural vibration frequencies and mode shapes of the curved shell. As mentioned before, a ratio E_L/E_R is set for analysis, where the Young's modulus of the research object is fixed as aluminum. Five different values of E_L/E_R are chosen as 1, 10, 500, 1000, 2000 and P_{inner} = 1MPa, θ=0.2, R_α=2540.01mm as shown in Fig.3 and Fig.4. First, the case E_L/E_R = 1 is discussed. Figures 3(a) and Fig.3(c) report the first 8 mode frequencies and the first 8 mode shapes for P_{axial} = 0MPa, respectively. In Fig.3(a), the frequencies of mode 1 and mode 3 decrease with the increase of P_{axial}. When P_{axial} reaches the critical point, the first buckling comes from mode 1. Moreover, one parabolic phenomenon of mode 1 and the veering between mode 5 and mode 6 are recognized in Fig.3(b).

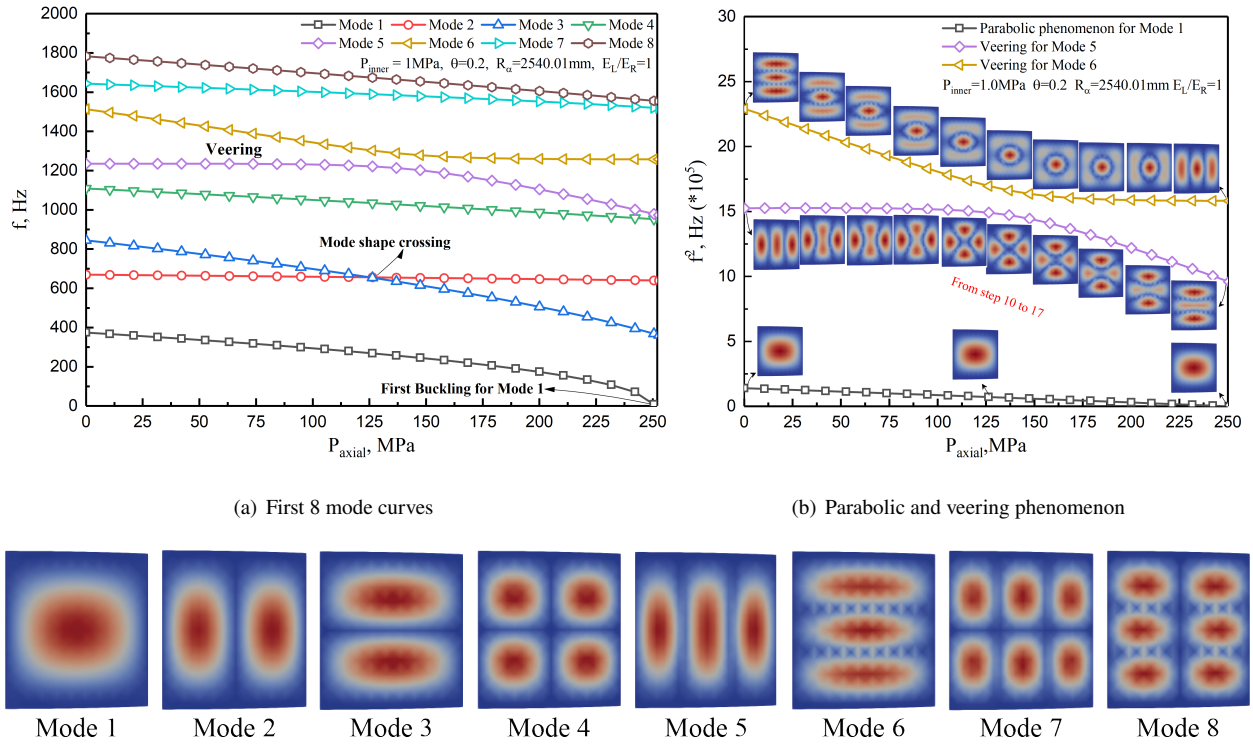

(a) First 8 mode curves

(b) Parabolic and veering phenomenon

(c) First 8 mode shapes of $E_L/E_R = 1$ for $P_{axial} = 0$MPa

Fig. 3 Effect of the loading part especially when $E_L/E_R = 1$, $P_{inner} = 1$MPa, $\theta = 0.2$, $R_\alpha = 2540.01$mm.

Then, the frequency curves of first three modes for different E_L/E_R are illustrated in Fig.4. For condition $P_{inner} = 1$MPa, $\theta = 0.2$ and $R_\alpha = 2540.01$mm, we can find that for these 4 ratios, all the buckling axial compression loads come from mode 1. The E_L/E_R makes a difference to the vibration frequencies of the shell. The convergence that the first 3 frequency curves keeps unchanged, when the ratio E_L/E_R =500, 1000 and 2000, is illustrated in Fig.4 as well. Since a uniform pressure has to be applied to the research object, it is not an ideal way to impose point load on each nodes of the side surface to generate uniform pressure in terms of numerical simulation. On the other hand, the side surface of the curved shell can't always keep as a smooth surface with directly applied the axial compression on the sides in real situation. Some unpredictable conditions, such as shrinking or expansion, occurs during the loading process. By means of attaching loading parts to the research object, the unpredictable condition that might occurred on the sides is eased and transferred to the loading part. In that case, a point load on the middle point of the side surface of the loading part and choosing a proper ratio E_L/E_R are theoretically enough to generate the uniform pressure. In Fig.5, different stress conditions on the sides after adding the loading parts for different E_L/E_R are illustrated. Clearly, lower E_L/E_R results in the stress concentration and irregular displacements in axial direction. Combing Fig.4 and Fig.5, E_L/E_R =1000 is bigger enough to generate uniform axial pressure to the research object.

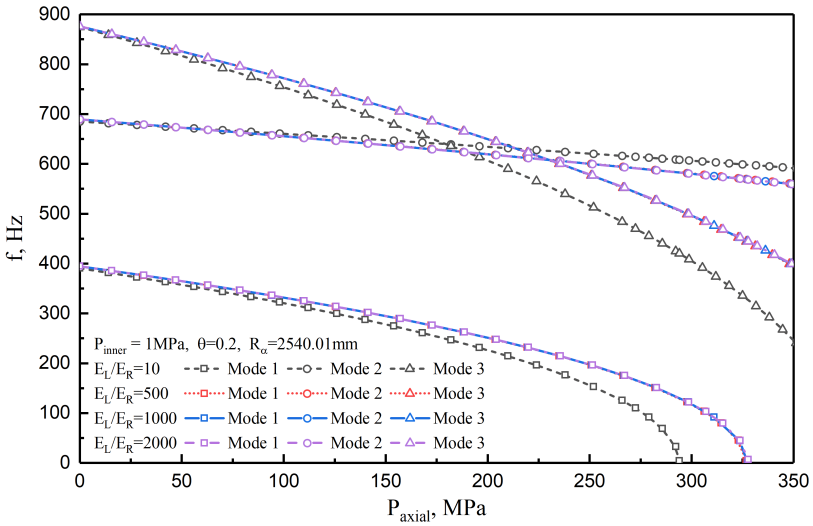

Fig. 4 First 3 mode frequency curves for different E_L/E_R with fixed P_{inner} = 1MPa, θ = 0.2, R_α = 2540.01mm.

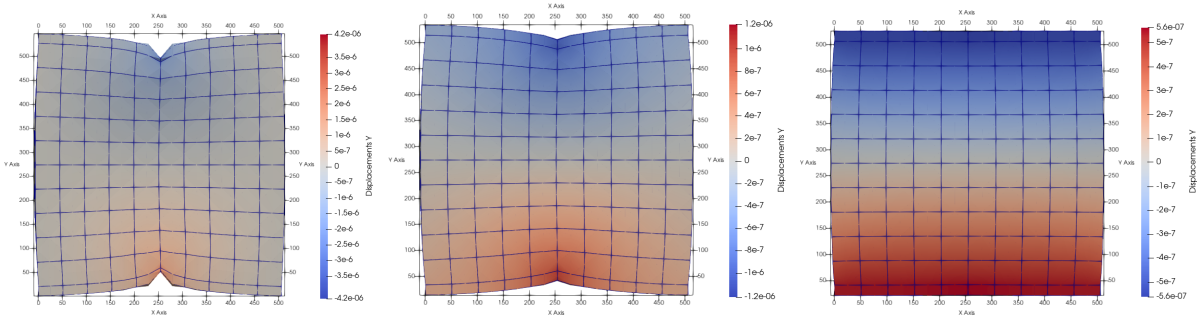

(a) E_L/E_R = 1 (b) E_L/E_R = 10 (c) E_L/E_R = 500

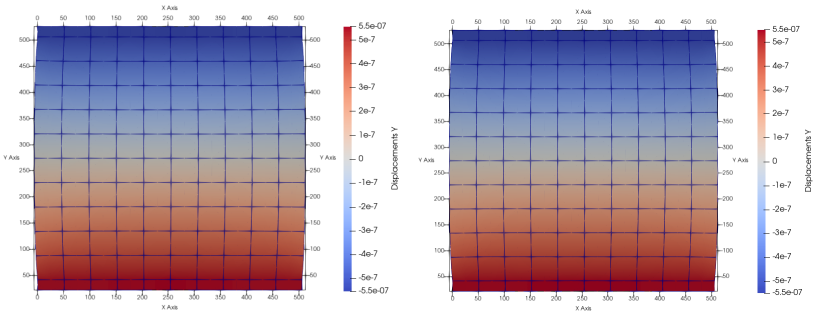

(d) E_L/E_R = 1000 (e) E_L/E_R = 2000

Fig. 5 Static analyzed Mode shapes for increasing E_L/E_R with fixed P_{inner} = 1MPa, θ = 0.2, R_α = 2540.01mm.

B. Effect of the changing inner pressure (P_{inner}).

In this section, it is studied how the P_{inner} affects the frequencies of the isotropic curved panel. The same properties are used as $E_l = 70.0 \times 10^6\,\mathrm{N/mm^2}$(i.e. E_L/E_R = 1000), θ=0.2, R_α=2540.01mm. Four different values of P_{inner},

i.e. 0MPa, 0.1MPa, 0.5MPa and 1MPa, are chosen and the corresponding first mode shapes and the relevant veering phenomena are shown from Fig.6 to Fig.9.

For these 4 different P_{inner}, first buckling comes from mode 1 and mode shape crossing occurs between mode 2 and mode 3, mode 7 and mode 8. The corresponding mode shapes are illustrated in Figs.6(c), 7(c) and 8(c) as well. Something interesting is that when we increase the P_{inner} to 0.5MPa, veering between mode 5 and mode 6 starts appearing. In Fig.9, the larger P_{inner} = 1 MPa makes the veering more obvious as the gap between these two lines becoming wider.

Combining these four figures, it can be stated that the frequencies of first 8 modes decrease with the increase of P_{axial} for different P_{inner}. Meanwhile, the plotted first and second buckling axial compression load increase with the increase of the P_{inner}. However, the change of the P_{inner} makes no difference to the basic mode shapes for P_{axial} = 0MPa by comparing Figs. 6(c), 7(c), 8(c) and 9(c). Fig.10 shows the first 3 modes curves for different P_{inner} in one plot. Clearly, the application of the P_{inner} increases the overall vibration frequencies. In Fig.9(b), veering occurs between mode 5 and mode 6 and the mode shapes between mode 5 and mode 6 start switching from steps 17 to 23.

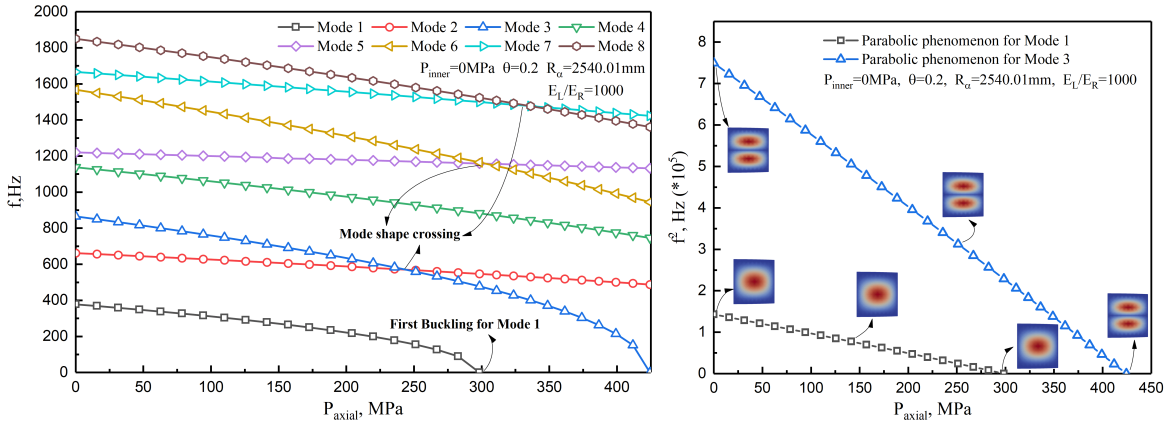

(a) First 8 mode curves

(b) Parabolic phenomenon for mode 1 and mode 3

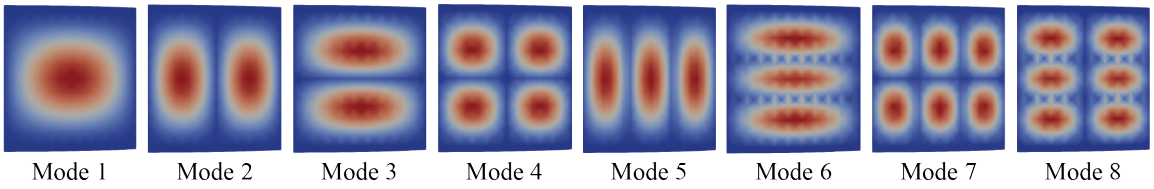

(c) First 8 mode shapes for P_{axial} = 0MPa

Fig. 6 First 8 mode curves, mode shapes and complete parabolic phenomenon for P_{inner} = 0MPa, θ = 0.2, R_α = 2540.01mm **and** E_L/E_R = 1000.

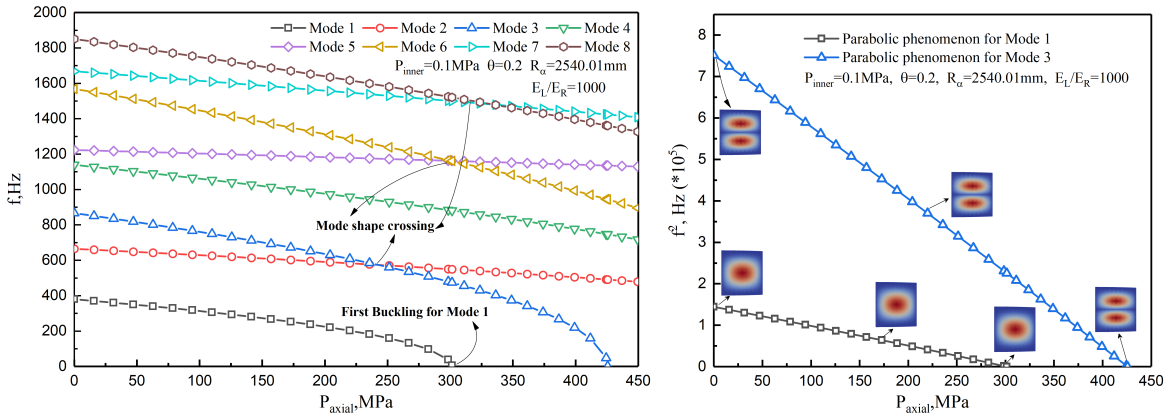

(a) First 8 mode curves

(b) Parabolic phenomenon for mode 1 and mode 3

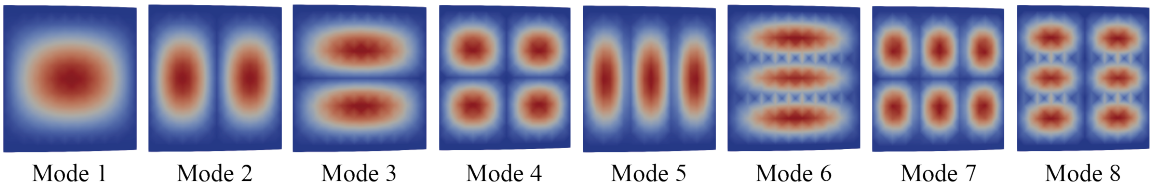

(c) First 8 mode shapes for P_{axial} = 0MPa

Fig. 7 First 8 mode curves, mode shapes and complete parabolic phenomenon for P_{inner} = 0.1MPa, θ = 0.2, R_α = 2540.01mm **and** E_L/E_R = 1000

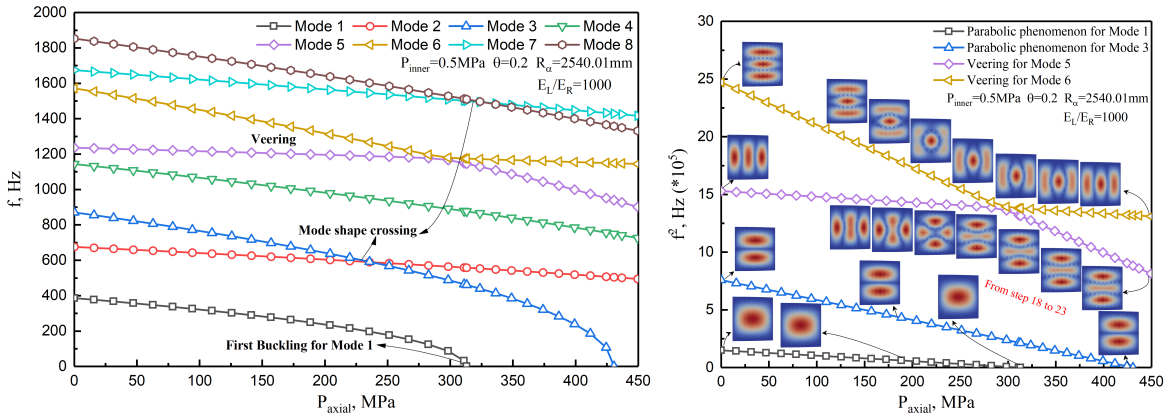

(a) First 8 mode curves

(b) Parabolic phenomenon for mode 1 and mode 3

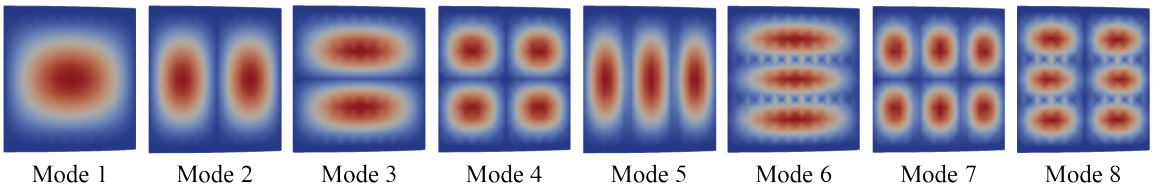

(c) First 8 mode shapes for P_{axial} = 0MPa

Fig. 8 First 8 mode curves, mode shapes and complete parabolic phenomenon for P_{inner} = 0.5MPa, θ = 0.2, R_α = 2540.01mm **and** E_L/E_R = 1000

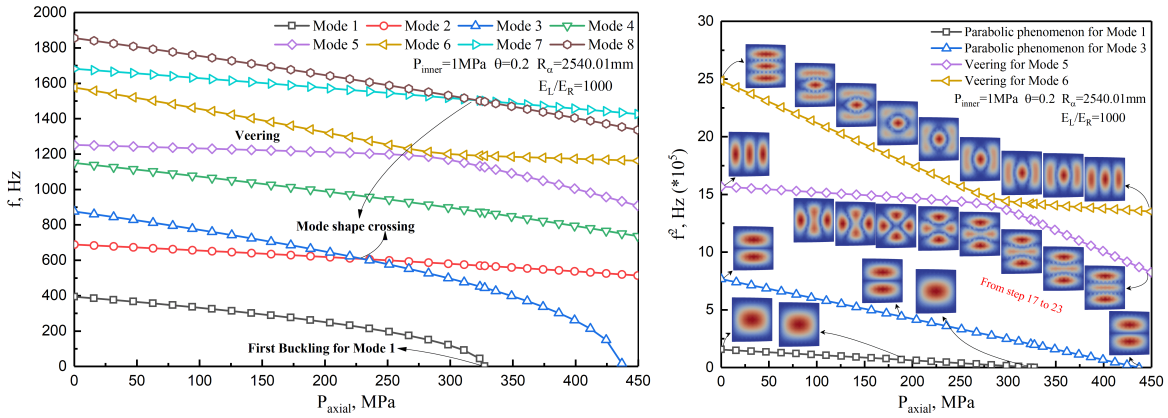

(a) First 8 mode curves

(b) Parabolic and veering phenomenon

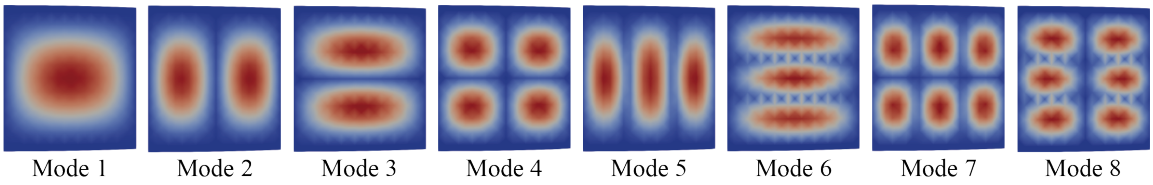

(c) First 8 mode shapes for P_{axial} = 0MPa

Fig. 9 First 8 mode curves, mode shapes and complete parabolic phenomenon for P_{inner} = 1MPa, θ = 0.2, R_α = 2540.01mm **and** E_L/E_R = 1000

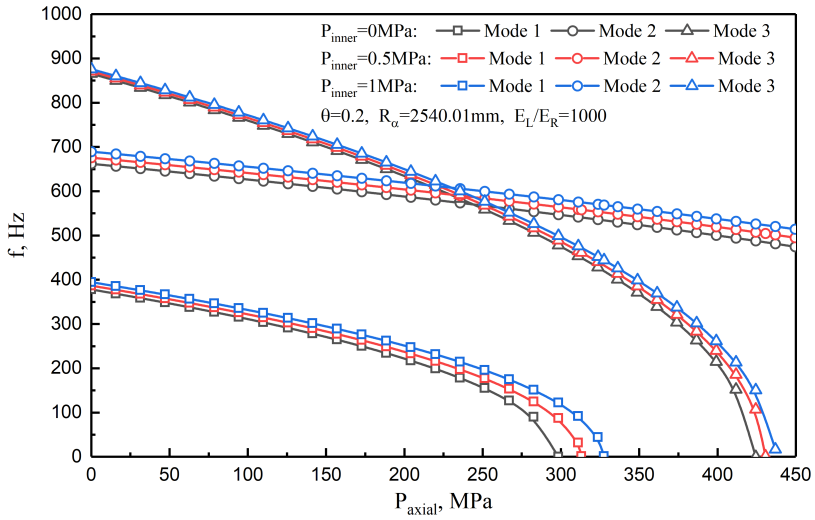

Fig. 10 First 3 mode curves for different Inner Pressure (P_{inner} = 0, 0.5, 1MPa)**.**

Next, the Modal Assurance Criterion (MAC) analysis is used to determine the similarity of two mode shapes. In case of same mode shapes (i.e., all points move the same) MAC shows black squares on the main diagonal; otherwhise, if the mode shapes are different, MAC displays grey boxes spread in the graph. Referring to the plots from Fig. 6 to Fig. 9, cprresponding MAC number are shown from Fig.11 to Fig. 14, respectively. In Fig.11 reports the mode shapes at

step 1 vs mode shapes in step 10, first buckling and second buckling loads. Fig.11(a) shows that the mode shapes for P_{axial}=0MPa are identical to the mode shapes for step 10. Fig. 11(b) exhibits the mode shape crossing between mode 2 and mode 3 and Fig. 11(c) exhibits the mode shape crossing between mode 2 and mode 3, mode 5 and mode 6, mode 7 and mode 8 comparing with Fig.6. Similar conclusions can be drawn from Figs. 12 and 13. However, a veering phenomenon between mode 5 and mode 6 is recorded in Fig.9.

Fig. 14(c) shows the veering progress between mode 5 and mode 6 from calculating step 17 to calculating step 22. Figure 14(a) show the MAC number between mode shapes for P_{axial}=0MPa and mode shapes of calculating step 24, where calculating step 19 is exactly in the veering progress. Fig.14(b) shows the MAC number after veering.

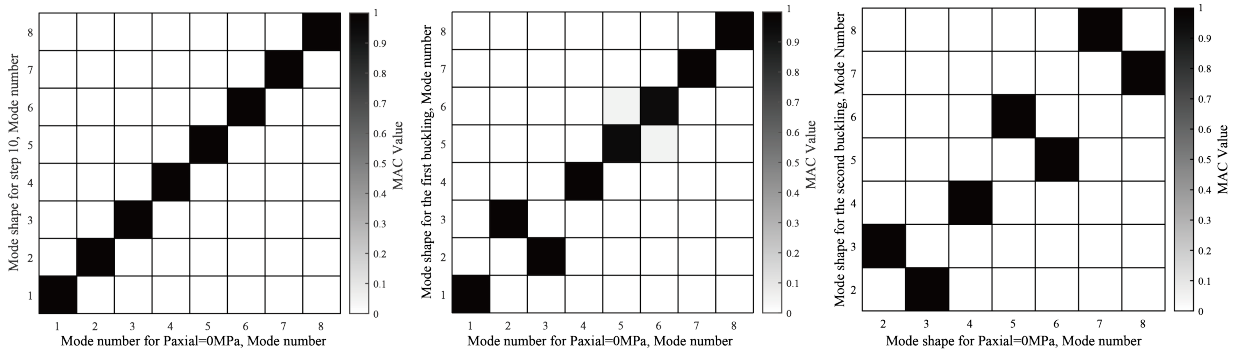

(a) Step 1 vs Step 10 (b) Step 1 vs First buckling (c) Step 1 vs Second buckling

Fig. 11 MAC number for P_{inner} = 0MPa**,** θ = 0.2**,** R_α = 2540.01mm **and** E_L/E_R = 1000

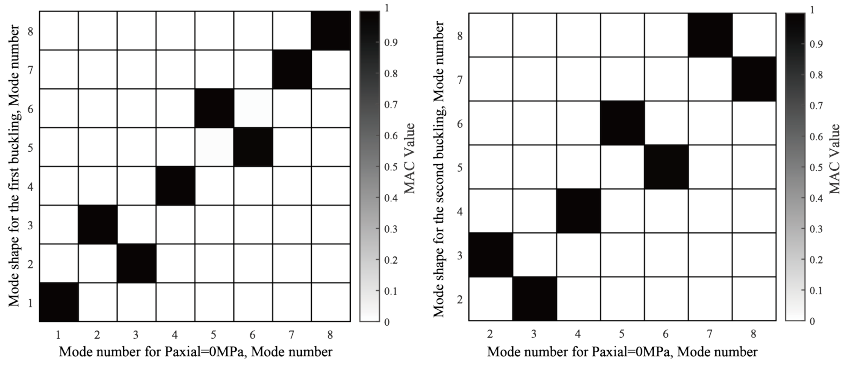

(a) Step 1 vs First buckling (b) Step 1 vs Second buckling

Fig. 12 MAC number for P_{inner} = 0.1MPa**,** θ = 0.2**,** R_α = 2540.01mm **and** E_L/E_R = 1000

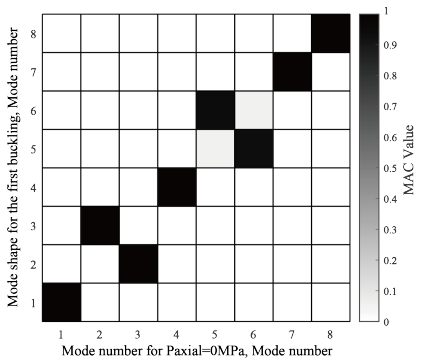

(a) Step 1 vs first buckling

Fig. 13 MAC number for P_{inner} = 0.5MPa**,** θ = 0.2**,** R_α = 2540.01mm **and** E_L/E_R = 1000

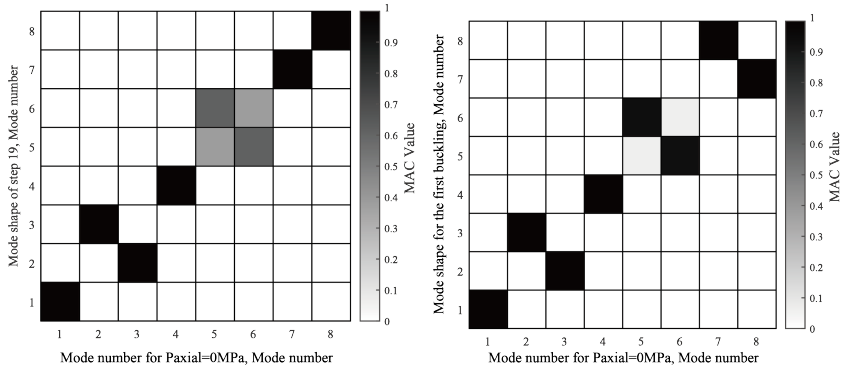

(a) Step 1 vs Step 19 (b) Step 1 vs First buckling

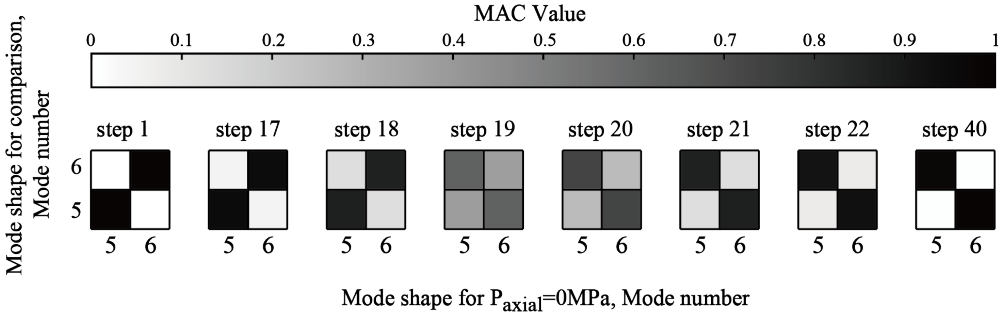

(c) Veering for mode 5 and 6

Fig. 14 MAC number for P_{inner} = 1MPa**,** θ = 0.2**,** R_α = 2540.01mm **and** E_L/E_R = 1000

C. Effect of different Radius(R_α) and central angle(θ).

In this section, it is discussed how different curvatures affect the natural frequencies of the isotropic curved shell. Here, we divide the impact factor into two parts that is the Radius (R_α) and the central angle (θ) by means of arc length

formula

$$\text{Arc Length} = \theta \times R_\alpha. \tag{11}$$

As is shown in Fig.15, three different kinds of parameters($\theta = 0.2$ and $R_\alpha = 2540.01$mm; $\theta = \Pi/8$ and $R_\alpha = 1293.61$mm; $\theta = \Pi/4$ and $R_\alpha = 646.81$mm) are chosen to represent different curvatures. Moreover, two different P_{inner}(i.e. P_{inner}=0MPa, 0.5MPa) are chosen for comparison. Figures 15(a) and 15(b) show that the natural frequencies decrease with the increase of P_{axial}. For the first 2 small curvature cases (i.e. θ=0.2, R_α=2540.01mm and θ=$\Pi/8$, R_α=1293.61mm), buckling comes from first natural frequency. When the curvature increases(i.e. θ=$\Pi/4$, R_α=646.81mm), buckling comes from the third natural frequency. Moreover, the buckling load of the curved shell with small curvature is lower than that with large curvature which means that curved shels with bigger curvature buckle earlier.

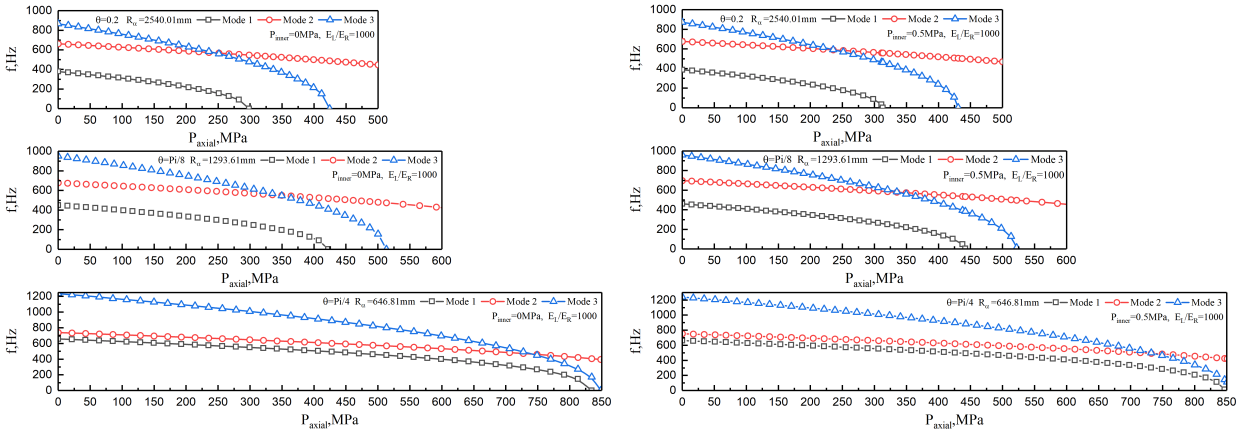

(a) First 3 mode curves for P_{inner} = 0MPa

(b) First 3 mode curves for P_{inner} = 0.5MPa

Fig. 15 Effect of 3 kinds of central angle (θ) and Radius(R_α) under two kinds of P_{inner}=0MPa & 0.5MPa with fixed E_L/E_R =1000.

V. Conclusion

In this paper, we discussed the change of the natural frequency and the relevant mode shapes of an isotropic metallic curved shell subjected to combined internal pressure and axial compression by means of 3 impact factors: E_L/E_R, P_{inner}, R_α and θ. We can state that the proposed model is capable of describing the vibration characteristics of the metallic curved shells under combined loading conditions without reaching its instability points. Different values of E_L/E_R simulate different loading conditions in real working situations and the adoption of the loading part with high E_L/E_R attached to the metallic curved shells ensures the successful application of uniform axial compression. Features like mode shape crossing/change, parabolic phenomenon and veering for different cases of P_{inner} are illustrated. Additionally, higher P_{inner} leads to higher buckling load. The study on effect of different radius(R_α) and central angle(θ) shows that shells with small curvatures bucks easier than that with large curvatures.

Acknowledgments

The work is supported by the National Natural Science Foundation of China (No. 11872329), the Natural Science Foundation of Zhejiang Province (No. LD21A020001), the 111 Project (No. B21034), and the Shenzhen Scientic and Technological Fund for R&D, PR China (No. 2021Szvup152) are also acknowledged. Fangzhou Zhu was sponsored by the China Scholarship Council (No.202006320363) to study at Politecnico di Torino.

References

[1] Augustine, B., et al., "Stress analysis and progressive failure Analysis of multilayered Basalt/Epoxy composites," *Applied Mechanics and Materials*, Vol. 766, Trans Tech Publ, 2015, pp. 21–26.

[2] Huey, D., Hair, J., and McLeod, K. B., "Installation loading and stress analysis involved with pipelines installed by horizontal directional drilling," Tech. rep., North American Society for Trenchless Technology, Chicago, Illinois, USA., 1996.

[3] Parnas, L., and Katırcı, N., "Design of fiber-reinforced composite pressure vessels under various loading conditions," *Composite structures*, Vol. 58, No. 1, 2002, pp. 83–95.

[4] Abramovich, H., Govich, D., and Grunwald, A., "Buckling prediction of panels using the vibration correlation technique," *Progress in Aerospace Sciences*, Vol. 78, 2015, pp. 62–73.

[5] Kepple, J., Herath, M., Pearce, G., Prusty, G., Thomson, R., and Degenhardt, R., "Improved stochastic methods for modelling imperfections for buckling analysis of composite cylindrical shells," *Engineering Structures*, Vol. 100, 2015, pp. 385–398.

[6] Wagner, H., Hühne, C., Niemann, S., and Khakimova, R., "Robust design criterion for axially loaded cylindrical shells-Simulation and Validation," *Thin-Walled Structures*, Vol. 115, 2017, pp. 154–162.

[7] Hilburger, M. W., "On the development of shell buckling knockdown factors for stiffened metallic launch vehicle cylinders," *2018 AIAA/ASCE/AHS/ASC structures, structural dynamics, and materials conference, Kissimmee, Florida, USA.*, 2018, p. 1990.

[8] Hess, T., "Stability of orthotropic cylindrical shells under combined loading," *ARS Journal*, Vol. 31, No. 2, 1961, pp. 237–246.

[9] Cheng, S., and Ho, B., "Stability of heterogeneous aeolotropic cylindrical shells under combined loading," *AIAA Journal*, Vol. 1, No. 4, 1963, pp. 892–898.

[10] Pope, G., "On the axial compression of long, slightly curved panels," *Aeronautical Research Council Reports & Memoranda*, 1963.

[11] Tamate, H., O.and Sekine, "Postbuckling behavior of thin curved panels under axial compression," *Bulletin of JSME*, Vol. 12, No. 51, 1969, pp. 415–420.

[12] Shen, H.-S., and Chen, T.-Y., "Buckling and postbuckling behaviour of cylindrical shells under combined external pressure and axial compression," *Thin-walled structures*, Vol. 12, No. 4, 1991, pp. 321–334.

[13] Shen, H.-S., "Postbuckling of shear deformable cross-ply laminated cylindrical shells under combined external pressure and axial compression," *International Journal of Mechanical Sciences*, Vol. 43, No. 11, 2001, pp. 2493–2523.

[14] Lam, K. Y., and Ng, T. Y., "Dynamic stability of cylindrical shells subjected to conservative periodic axial loads using different shell theories," *Journal of Sound and Vibration*, Vol. 207, No. 4, 1997, pp. 497–520.

[15] Bisagni, C., and Cordisco, P., "An experimental investigation into the buckling and post-buckling of CFRP shells under combined axial and torsion loading," *Composite Structures*, Vol. 60, No. 4, 2003, pp. 391–402.

[16] Mehralian, F., Beni, Y. T., and Ansari, R., "On the size dependent buckling of anisotropic piezoelectric cylindrical shells under combined axial compression and lateral pressure," *International Journal of Mechanical Sciences*, Vol. 119, 2016, pp. 155–169.

[17] Jansen, E., Abramovich, H., and Rolfes, R., "The direct prediction of buckling loads of shells under axial compression using VCT-towards an upgraded approach," *29th congress on the International Council of the Aeronutical Science*, 2014, pp. 1–9.

[18] Kalnins, K., Arbelo, M. A., Ozolins, O., Skukis, E., Castro, S. G., and Degenhardt, R., "Experimental nondestructive test for estimation of buckling load on unstiffened cylindrical shells using vibration correlation technique," *Shock and Vibration*, Vol. 2015, 2015.

[19] Sommerfeld, A., "A simple device to illustrate the buckling process," *Magazine of the Association of German Engineers (ZVDI)*, 1905, pp. 1320–1323.

[20] Föppl, L., "Bestimmung der Knicklast eines Stabes aus Schwingungsversuchen," *Beiträge zur technischen Mechanik und technischen Physik*, Springer, 1924, pp. 82–88.

[21] Hohenemser, K. H., and Prager, W., *Dynamik der Stabwerke*, Springer, 1933.

[22] Stephens, B. C., "Natural vibration frequencies of structural members as an indication of end fixity and magnitude of stress," *Journal of the Aeronautical Sciences*, Vol. 4, No. 2, 1936, pp. 54–60.

[23] Massonnet, C. E., *Les relations entre les modes normaux de vibration et la stabilité des systèmes élastiques*, Goemaere, 1940.

[24] Lurie, H., "Effective end restraint of columns by frequency measurements," *Journal of the Aeronautical Sciences*, Vol. 18, No. 8, 1951, pp. 566–567.

[25] Lurie, H., "Lateral vibrations as related to structural stability," 1952.

[26] Singer, J., Arbocz, J., Weller, T., and Cheney, J., "Buckling Experiments: Experimental Methods in Buckling of Thin-Walled Structures. Shells, Built-up Structures, Composites and Additional Topics, Volume 2," *Appl. Mech. Rev.*, Vol. 56, No. 1, 2003, pp. B5–B5.

[27] Arbelo, M. A., Kalnins, K., Ozolins, O., Skukis, E., Castro, S. G., and Degenhardt, R., "Experimental and numerical estimation of buckling load on unstiffened cylindrical shells using a vibration correlation technique," *Thin-Walled Structures*, Vol. 94, 2015, pp. 273–279.

[28] Skukis, E., Ozolins, O., Kalnins, K., and Arbelo, M. A., "Experimental test for estimation of buckling load on unstiffened cylindrical shells by vibration correlation technique," *Procedia Engineering*, Vol. 172, 2017, pp. 1023–1030.

[29] Shahgholian-Ghahfarokhi, D., and Rahimi, G., "Buckling load prediction of grid-stiffened composite cylindrical shells using the vibration correlation technique," *Composites Science and Technology*, Vol. 167, 2018, pp. 470–481.

[30] Labans, E., Abramovich, H., and Bisagni, C., "An experimental vibration-buckling investigation on classical and variable angle tow composite shells under axial compression," *Journal of Sound and Vibration*, Vol. 449, 2019, pp. 315–329.

[31] Tian, K., Huang, L., Yang, M., Chen, Y., Hao, P., and Wang, B., "Concurrent numerical implementation of vibration correlation technique for fast buckling load prediction of cylindrical shells under combined loading conditions," *Engineering with Computers*, 2021, pp. 1–13.

[32] Franzoni, F., Odermann, F., Wilckens, D., Skuķis, E., Kalniņš, K., Arbelo, M. A., and Degenhardt, R., "Assessing the axial buckling load of a pressurized orthotropic cylindrical shell through vibration correlation technique," *Thin-Walled Structures*, Vol. 137, 2019, pp. 353–366.

[33] Pagani, A., Augello, R., and Carrera, E., "Virtual Vibration Correlation Technique (VCT) for Nonlinear Analysis of Metallic and Composite Structures," *ASME International Mechanical Engineering Congress and Exposition*, Vol. 52002, American Society of Mechanical Engineers, 2018.

[34] Azzara, R., Carrera, E., and Pagani, A., "Nonlinear and linearized vibration analysis of plates and shells subjected to compressive loading," *International Journal of Non-Linear Mechanics*, Vol. 141, 2022, p. 103936.

[35] Yang, H., Daneshkhah, E., Augello, R., Xu, X., and Carrera, E., "Numerical vibration correlation technique for thin-walled composite beams under compression based on accurate refined finite element," *Composite Structures*, 2021, p. 114861.

[36] Carrera, E., Pagani, A., Azzara, R., and Augello, R., "Vibration of metallic and composite shells in geometrical nonlinear equilibrium states," *Thin-Walled Structures*, Vol. 157, 2020, p. 107131.

[37] Wu, B., Pagani, A., Chen, W., and Carrera, E., "Geometrically nonlinear refined shell theories by Carrera Unified Formulation," *Mechanics of Advanced Materials and Structures*, 2019, pp. 1–21.

[38] Carrera, E., Cinefra, M., Petrolo, M., and Zappino, E., *Finite element analysis of structures through unified formulation*, John Wiley & Sons, 2014.

[39] Bathe, K.-J., *Finite element procedures*, New Yersey, 1996.

[40] Pagani, A., and Carrera, E., "Unified formulation of geometrically nonlinear refined beam theories," *Mechanics of Advanced Materials and Structures*, Vol. 25, No. 1, 2018, pp. 15–31.